UNIVERSITY *of York*

This is a repository copy of *Comparing antiviral strategies against COVID-19 via multiscale within-host modelling*.

White Rose Research Online URL for this paper:
https://eprints.whiterose.ac.uk/182143/

Version: Published Version

Article:

White Rose
university consortium
Universities of Leeds, Sheffield & York

eprints@whiterose.ac.uk
https://eprints.whiterose.ac.uk/

Research

Author for correspondence:
R. Twarock
e-mail: rt507@york.ac.uk

Comparing antiviral strategies against COVID-19 via multiscale within-host modelling

F. Fatehi[1,2], R. J. Bingham[1,2,3], E. C. Dykeman[1,2], P. G. Stockley[4] and R. Twarock[1,2,3]

[1]Department of Mathematics, [2]York Cross-disciplinary Centre for Systems Analysis, and [3]Department of Biology, University of York, York YO10 5DD, UK
[4]Astbury Centre for Structural Molecular Biology, Faculty of Biological Sciences, University of Leeds, Leeds LS2 9JT, UK

FF, 0000-0003-3743-5772; RJB, 0000-0001-5140-269X; ECD, 0000-0002-8344-8446; PGS, 0000-0002-1360-2751; RT, 0000-0002-1824-2003

Within-host models of COVID-19 infection dynamics enable the merits of different forms of antiviral therapy to be assessed in individual patients. A stochastic agent-based model of COVID-19 intracellular dynamics is introduced here, that incorporates essential steps of the viral life cycle targeted by treatment options. Integration of model predictions with an intercellular ODE model of within-host infection dynamics, fitted to patient data, generates a generic profile of disease progression in patients that have recovered in the absence of treatment. This is contrasted with the profiles obtained after variation of model parameters pertinent to the immune response, such as effector cell and antibody proliferation rates, mimicking disease progression in immunocompromised patients. These profiles are then compared with disease progression in the presence of antiviral and convalescent plasma therapy against COVID-19 infections. The model reveals that using both therapies in combination can be very effective in reducing the length of infection, but these synergistic effects decline with a delayed treatment start. Conversely, early treatment with either therapy alone can actually increase the duration of infection, with infectious virions still present after the decline of other markers of infection. This suggests that usage of these treatments should remain carefully controlled in a clinical environment.

1. Introduction

COVID-19 is a recently emerging infectious disease caused by severe acute respiratory syndrome coronavirus 2 (SARS-CoV-2) [1]. After

outbreaks of severe acute respiratory syndrome coronavirus (SARS-CoV) in 2002, and of Middle East respiratory syndrome coronavirus (MERS-CoV) in 2012, this is the third outbreak of a coronavirus since the turn of the century. Mathematical models of COVID-19 transmission at the population level have been instrumental in controlling the spread of the virus, but a detailed understanding of within-host infection dynamics is still lacking. Like SARS-CoV and MERS-CoV, SARS-CoV-2 is a betacoronavirus in Group IV of the Baltimore classification of viruses. Compared with other single-stranded (ss)RNA viruses, coronaviruses have the longest genomes. The smallest RNA viruses, for example, are only approximately 1–4 kb in length, and HIV has two copies of an approximately 10 kb genome, while the SARS-CoV-2 genome is a positive-sense, ssRNA molecule of approximately 30 kb. As a consequence, the viral life cycle of coronaviruses is distinct from most other ssRNA viruses, and existing intracellular infection models, e.g. for hepatitis C virus [2], cannot be applied here. Therefore, we introduce here a novel intracellular model of SARS-CoV-2 infection that incorporates essential steps specific to coronaviral life cycles. This model enables us to study in detail the viral dynamics inside an infected cell, and provides a framework to study the impacts of antiviral treatments on the infection dynamics within an infected cell. In particular, it enables us to quantify the impact of different treatment options on the viral load that is secreted from an infected cell.

Outcomes from the intracellular model are then integrated into an intercellular model, that takes the impact of the immune response on infection dynamics within an infected individual into account. The model has been parametrized with data from 12 patients from a study in Singapore [3], enabling us to generate a generic profile of disease progression in patients that have recovered from the disease. Model predictions agree well with experimentally and clinically measured parameters such as the duration of the *incubation period*, suggesting that this scenario is representative of disease progression seen in COVID-19 patients. We then use this model to study the infection dynamics in patients with different levels of immune responses by varying parameters associated with the immune response, such as the proliferation rates of effector cells and antibodies, and the rate by which effector cells remove infected cells. Comparison of different scenarios is based on tissue damage and viral load, highlighting the impact(s) of antibodies and adaptive cell-mediated immune response on infection dynamics.

This provides a framework in which to compare the impacts of different forms of antiviral therapy and assess their synergies. We focus here on two prominent forms of therapy against COVID-19: remdesivir, that inhibits virus production within an infected cell [4], and convalescent plasma (CP) therapy, whereby CP derived from recently recovered donors is transfused to the patients as an additional support [5]. Recent studies have concluded that remdesivir is an effective antiviral treatment option for COVID-19 [4]. However, the rapid spread and novel nature of the disease make the detailed evaluation of effective treatment protocols difficult. Using mathematical models enables us to study in detail the effect of the drug remdesivir on viral load in a COVID-19 infection. Gonçalves *et al.* used a 'target-cell limited' model to evaluate the efficacy of different treatment options against SARS-CoV-2 infections [6]. They showed that if drugs such as remdesivir are administered very early, this may help control viral load, but may not have a major effect in severely ill patients. Iwanami *et al.* also introduced a mathematical model to describe the within-host viral dynamics of SARS-CoV-2 and demonstrated that late timing of treatment initiation can mask the effect of antivirals in clinical studies of COVID-19 [7]. However, none of these models have included the impact of the immune response directly into their model, which plays an important role in the outcomes of the infection. In order to analyse different aspects of viral dynamics, studying the interactions between viruses and the immune system of the host is crucial [8,9]. In this work, we take the impact of the immune response on infection dynamics into account to perform a more robust analysis of different treatment options. Regarding the CP therapy, several studies performed in various countries have shown that this treatment is effective against COVID-19 infections and its safety has been well established in a randomized clinical trial (RCT) on a large population [5,10–15]. However, finding the optimal dose and time for CP therapy is still debated [5]. Our intercellular model provides insights into the effects of different dosages and treatment starts in terms of infection-related quantities for CP therapy and this supports efforts in combating the COVID-19 pandemic.

2. Results

2.1. An *in silico* model of intracellular SARS-CoV-2 infection dynamics

Our stochastic model of viral infection dynamics within an infected host cell tracks the different viral and cellular components required for formation of progeny virus. These include the structural proteins that make up the virus: the envelope (E) protein, the membrane (M) protein, and the spike (S) protein, as well
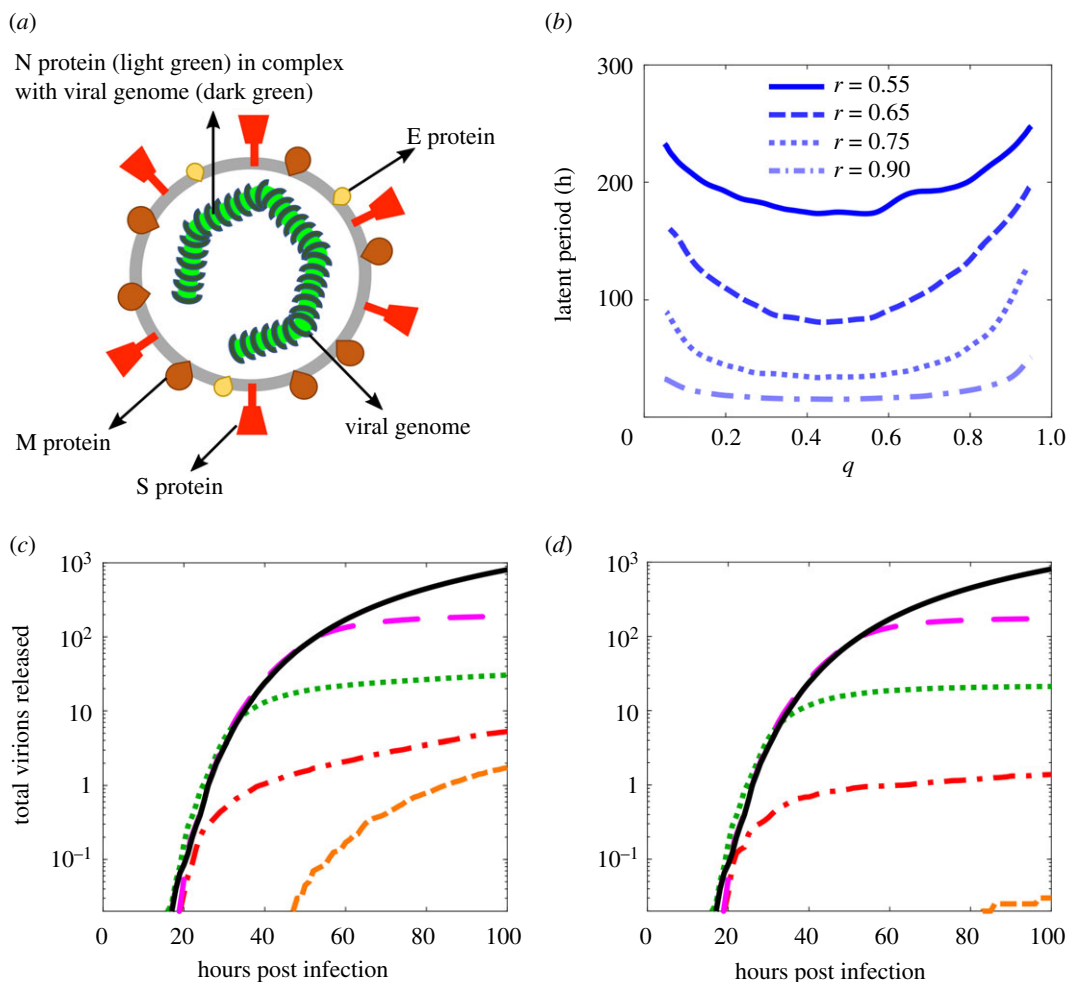
Figure 1. An earlier treatment start, especially during the latent period, is more effective. (*a*) Illustration of a SARS-CoV-2 virion; the viral genome (dark green) is in complex with nucleocapsid (N) protein (light green) and is enclosed by the viral envelope that is studded by other structural glycoproteins, the spike (S) protein (red), the membrane (M) protein (maroon) and the envelope (E) protein (yellow). (*b*) Time lag before the release of the first virion from an infected cell; the maximal release of virions occurs when the replicase–transcriptase complex (RTC) elongation probability, r, is high and the frameshifting rate, q, is between 0.3 and 0.5. (*c*, *d*) Profiles of viral load from an infected cell after introducing treatment at different times post infection, for a concentration of 25 (*c*) and 50 (*d*) molecules of remdesivir, respectively. The black solid curve indicates the drug-free control. The magenta (long-dashed), green (dotted), red (dashed-dotted) and orange (dashed) curves correspond to a treatment start at 50, 30, 20 and 10 h post infection, respectively. Parameter values are given in electronic supplementary material, table S1.

as the nucleocapsid (N) protein (figure 1*a*). N protein forms a complex with the genomic RNA (gRNA), and thus aids its compaction for ease of packaging within the viral envelope. The S protein binds the angiotensin-converting enzyme 2 (ACE-2) receptor on human cells and is therefore essential for cell entry. The model also includes non-structural proteins that are important for the viral life cycle, such as the replicase–transcriptase complex (RTC), and keeps track of the numbers of gRNAs (and sub-genomic sgRNAs) at different stages of the replication process. These include both the original plus-sense template of the RNA molecules, as well as their negative-sense variants that arise transiently during transcription. There are nine negative-sense sub-genomic RNAs (–sgRNAs), corresponding to different gene products. In particular, there is an individual one for each of the structural proteins, allowing the virus to produce these components in the different quantities required for formation of viral particles [16].

The reactions modelling viral replication within the host cell are described in detail in the Methods section and the electronic supplementary material (SI). Here we provide a brief summary of the main reactions. The SARS-CoV-2 genome encodes two polyproteins, pp1a and pp1ab. The former is translated from the open reading frame ORF1a, and the latter from the overlapping reading frames 1a and 1b [17] via a −1 ribosomal frameshift during the translational elongation step. The relative

frequencies of occurrence of the ribosomal frameshift is a key mechanism of self-regulation of protein expression of the virus and hence an important parameter in our model, which is captured by the *frameshift probability q* [18].

Proteins cleaved from pp1a and pp1ab form the RTC, which is then used by the virus for genome replication and production of the nine (−)sgRNAs. (−)sgRNAs are produced through discontinuous transcription [19], where elongation of nascent (−)RNA continues until the first functional transcription-regulating sequence (TRS) is encountered. A fixed proportion of RTCs will disregard the TRS motif and continue to elongate the nascent strand, while the remainder will halt synthesis of the nascent minus strand and instead synthesize (−)sgRNAs [20]. The nine TRS motifs in the SARS-CoV-2 genome correspond to the nine sgRNAs produced, hence the choice to elongate or terminate synthesis occurs up to nine times during the elongation process [21]. The (−)RNA and (−)sgRNAs produce positive-sense RNAs by recruiting RTC. The sgRNAs are translated to form proteins using cellular ribosomes. In the final step, a gRNA and the structural proteins (S, M, N and E) form a new virion according to an assembly reaction that takes the stoichiometry of the different viral components into account [16], and the virus particle is then released from the host cell.

Stochastic simulations of the reactions were implemented using the Gillespie algorithm [22], and the number of particles released over the course of 100 h was computed as the average over 200 stochastic simulations. Parameter values used (electronic supplementary material, table S1) are predominantly based on experimentally available data [16,21,23–26]; for parameters for which no data were available, we ensured that our main conclusions are robust against their variation. In particular, the release rate of virions, following a time lag between infection of a host cell and its first release of viral particles, is constant and virions are secreted linearly (electronic supplementary material, figure S3).

We note, however, that the length of the time lag, and correspondingly the total number of virions released, are affected by some of these parameters and therefore warrant a more detailed investigation. For example, increasing the ribosomal protein production rate (electronic supplementary material, figure S3a) or the RTC nucleotide association rate (electronic supplementary material, figure S3b) decreases the time lag and therefore increases the number of virions released. By contrast, variation of the half-life of RTC or the formation rate of RTC from the constituent proteins does not have a significant effect on the time lag (electronic supplementary material, figure S3c and d). Figure 1b shows the time lag to the release of the first virion from an infected cell as a function of the ribosomal frameshifting probability q and of the RTC elongation probability r.

Figure 1b indicates that decreasing r results in a rapid increase in the time lag: for example, when $r = 0.55$ and the virus produces many sub-genomic fragments, this time lag is longer than 200 h. This implies that viral load is maximized for the scenario that the RTC favours continuation of the transcription process when encountering a TRS. Given the importance of frameshifting in the coronavirus life cycle to control the relative numbers of different viral components, it has been argued that the virus will have evolved to optimize this ratio. In particular, frameshift signals have been characterized experimentally previously to have efficiencies in the range of 20–45% [27–30], although a recent study has suggested that the frameshift rate may be slightly higher [31]. Our model identifies an optimal value of $0.3 < q < 0.5$ as the range with the lowest time lag and hence maximal virion release (figure 1b), in good agreement with the experimentally determined range of 20–45%.

2.2. The intracellular infection model in the presence and absence of antiviral therapy

In order to assess the impact of an antiviral drug on viral load in the context of the intracellular model, we use the example of remdesivir, which is a widely used treatment option against COVID-19. Remdesivir, originally developed as a treatment for hepatitis C virus and later trialled for efficacy against Ebola, acts as a nucleoside analogue that mimics adenosine nucleotide [32]. During the replication process, RTC may insert remdesivir molecules instead of adenosine, resulting in capping of the strand and thus terminating replication [25]. We have included additional reactions into the model that describe remdesivir binding to the RTC complexes on the gRNAs and sgRNAs to capture this (see electronic supplementary material for details), and track the effect of a given, fixed number of remdesivir molecules per cell on the release of viral particles from an infected host cell.

Figure 1c,d shows the impact on viral load released from a single-infected cell for two different concentrations of remdesivir, as well as treatment starts at different times post infection (TPIs). In figure 1c, a free concentration equivalent to 25 remdesivir molecules per cell is considered, corresponding to a concentration of approximately 0.06 µM (see electronic supplementary material) [26]. The black solid curve indicates the viral load in the absence of treatment as a control, computed as an average over 200

stochastic simulations of the model. Magenta (long-dashed), green (dotted), red (dashed-dotted) and orange (dashed) curves show the impact(s) of treatment start at TPIs of 50, 30, 20 and 10 h, respectively. Figure 1c demonstrates that starting treatment during the latent period reduces the total number of virions released significantly. Even given a later treatment start the rate of virion production is slowed down, but the earlier treatment is started, the stronger the reduction in the virion production rate. Our results are consistent with experiments that probed the impact of remdesivir on mouse hepatitis virus (MHV) infection [33], which also revealed that starting treatment earlier and during the latent period is more effective, as is the case also in other betacoronaviruses. Figure 1d shows the impact of doubling the drug concentration (equivalent to a concentration of 50 molecules of remdesivir per cell). In this case, starting treatment early during infection at 20 h post infection reduced the number of virions released on average by more than half. However, starting treatment later in the infection, such as 30 or 50 h post infection, decreases the number of released virions by a smaller fraction. This suggests that although an increased drug concentration can be beneficial, starting the treatment earlier is more effective at reducing viral load than an increase in dosage.

The intracellular model provides new insights into the release of viral particles from an infected cell, both in the absence and presence of antiviral treatment. The model shows that there is a time lag between infection of a host cell and the first release of new virions. It also shows that virions are effectively released linearly in time after the time lag which is not observed in other viral infections such as hepatitis B viral (HBV) infection [34]. The model reveals that antiviral therapy based on remdesivir has a higher efficacy in infected cells which are in the latent period compared with those that are already producing virions. We incorporated these facts in the next section into an intercellular model of within-host infection dynamics. The model can be used as a platform for comparing different therapeutic strategies that may develop in the future against COVID-19 infections [34].

2.3. Within-host model of SARS-CoV-2 infection dynamics

The intracellular model affords insights into the release of viral particles from an infected cell, both in the absence and presence of antiviral treatment. We integrate results from this model into an intercellular model of within-host infection dynamics in order to probe the impact of the adaptive immune response on disease progression both in the absence and presence of antiviral therapy. Uninfected target cells (T) are assumed to follow logistic growth with proliferation rate r_T and carrying capacity T_m. Inclusion of growth capacity of uninfected cells is important, because SARS-CoV-2 is detectable in patients over 20 days after the onset of symptoms [35], comparable to the time taken to regenerate the epithelium (up to one month [36]). Uninfected cells are infected by free virions at rate β. Although infected cells in the latent phase probably die at a somewhat lower rate than productively infectious cells, we assume that all infected cells die at approximately the same rate, δ, in order to minimize the number of free parameters that would complicate parameter estimation.

Our intracellular model shows a time lag between infection of a host cell and the first release of new virions, consistent with experimental observation [16]. This effect is included into our intercellular model via a latent phase (L) with a lifetime defined as $1/\gamma$, where γ denotes the average transition rate from the latent to the productively infectious (I) state, i.e. when the cell sheds viral particles. The intracellular model also shows that virions are effectively released linearly in time. Therefore, we model infected cells as producing new virions V at a constant production rate p, and assume that they are naturally cleared at rate c.

Our model of the adaptive immune response consists of antibodies A (humoral immune response) that remove virions at rate k, and effector cells E (cell-mediated immune response) that kill infected cells at rate μ, assuming the same rate for cells in the latent and infectious phase in order to minimize the number of free parameters. Antibodies are produced at rate p_A proportional to the viral load and are degraded at rate d_A. After viral clearance, the antibody level is kept at a homeostatic level, because of the long-lived plasma and memory B cells. To represent this, we add a logistic term with proliferation rate r_A and carrying capacity A_m to the antibody equation. A fixed basal level of effector cells is assumed (λ_E/d_E), and upon infection the population of effector cells will expand at rate $\alpha(L + I)E$ [37–39]. Both L and I have an impact on the immune response, because infected cells during the latent phase are producing viral proteins. Although infected cells at different stages of infection are likely to express slightly different levels of viral peptide-MHC (major histocompatibility complex) on their surface, we assumed that the rates are the same for L and I in order to minimize the number of free parameters in our model.
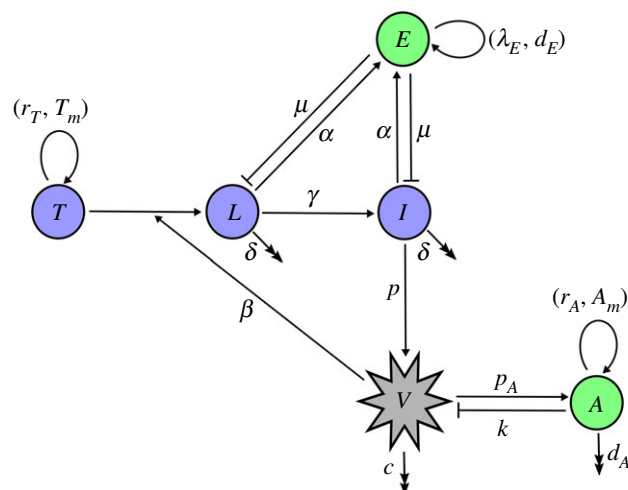
Figure 2. Diagram of the model of immune response to a viral infection. Purple circles show host cells (uninfected cells, infected cells in latent phase and productively infected cells), green circles indicated immune response (effector cells and free antibodies) and grey shows virions. Double arrow-headed lines show natural clearance. Bar-headed lines indicate the removal of infected cells and virions by immune response. Single arrow-headed lines show proliferation and production.

Considering the above assumptions, the model, as illustrated in figure 2, takes on the following form:

$$\frac{dT}{dt} = r_T T \left(1 - \frac{T + L + I}{T_m}\right) - \beta TV,$$

$$\frac{dL}{dt} = \beta TV - \delta L - \gamma L - \mu LE,$$

$$\frac{dI}{dt} = \gamma L - \delta I - \mu IE,$$

$$\frac{dV}{dt} = pI - cV - kAV,$$

$$\frac{dE}{dt} = \lambda_E + \alpha(L + I)E - d_E E,$$

$$\frac{dA}{dt} = p_A V + r_A A \left(1 - \frac{A}{A_m}\right) - kAV - d_A A.$$

(2.1)

The model was fitted to data from 12 hospitalized patients in Singapore [3] using measurements of viral load (see Methods). The parameter values derived from fitting V are presented in table 1. Our model captures essential features of the viral load in all patients, including the positions and heights of the first peak, and where applicable also those of the second peak (see electronic supplementary material, figure S4). In all patients, the viral load eventually decreases to below detectable levels, matching the clinical outcomes in these patients. We note that even details such as the slower viral decline in patients 2 and 12 are correctly represented by our model.

Our model predicts an *incubation period*, i.e. time between infection and presentation of symptoms, of 4.25 days (3.45–5.05 95% CI), in excellent agreement with the median SARS-CoV-2 *incubation period* of roughly 5 days estimated based on clinical data elsewhere [16,40]. The average time after which antibodies appear is predicted here to be 16 days (13.9–18.1 95% CI) after infection, again in excellent agreement with the clinically reported first detection of antibodies after 10–20 days [16]. Similarly, the *latent period* of 27.28 h (26.19–28.37 95% CI) predicted by our model agrees well with the experimentally observed latent period of 12–36 h [41].

2.4. Immune response dynamics

The within-host model enables the roles of different aspects of the adaptive immune response in viral clearance to be investigated in more detail. The adaptive immune response to a viral infection relies on both antibodies and effector T cells. In order to understand their respective contributions to viral

Table 1. Parameter best estimates. I.P., incubation period; A.A., antibodies appearance. The units of these parameters are day^{-1}.

patient	$\beta \times 10^{-8}$	δ	γ	μ	$p \times 10^{-3}$	$k \times 10^{-10}$	c	$\alpha \times 10^{-9}$	$p_A \times 10^{-5}$	r_A	I.P (day)	A.A (day)
1	20.7	0.248	0.9	0.047	2.18	2.37	1.24	17.2	1.33	1.98	4	15
2	2.54	0.248	0.9	0.00578	8.13	3.68	3.15	1.17	0.87	1.63	4	21
3	9.12	0.344	0.9	0.099	2.12	2.69	1.18	15.5	1.41	2.05	6	16
4	16.5	0.2	1	0.001	9.4	2.2	1.61	1.37	4.43	1.25	2	16
5	5.89	0.17	1	0.115	1.96	5.55	1.14	19.1	1.94	1.37	6	23
6	13	0.275	0.82	0.187	3.2	5	1.89	7.89	3.1	1.48	2	20
7	13.3	0.2	0.85	0.2	9.9	4.28	1.97	6.27	6.6	2.83	4	10
8	10.4	0.35	0.8	0.04	3.65	3.5	1.3	16.5	7	2.18	4	14
9	10.6	0.51	0.84	0.0035	10.4	2.8	1.1	0.86	0.96	2.13	3	13
10	12.2	0.229	0.8	0.12	10.2	2.66	3.91	3	5.65	1.57	6	16
11	12.5	0.2	0.9	0.067	1.3	4	0.75	8.09	6.5	2.5	6	13
12	6.07	0.2	0.9	0.001	9.31	1.26	1.7	1.12	7.7	1.98	4	14
median	11.4	0.239	0.9	0.057	5.89	3.15	1.46	7.08	3.77	1.98	4	15.5
mean	11.1	0.265	0.884	0.0739	5.98	3.33	1.75	8.17	3.96	1.91	4.25	16
s.d.	4.9	0.096	0.067	0.07	3.8	1.24	0.92	7.1	2.64	0.47	1.4	3.73
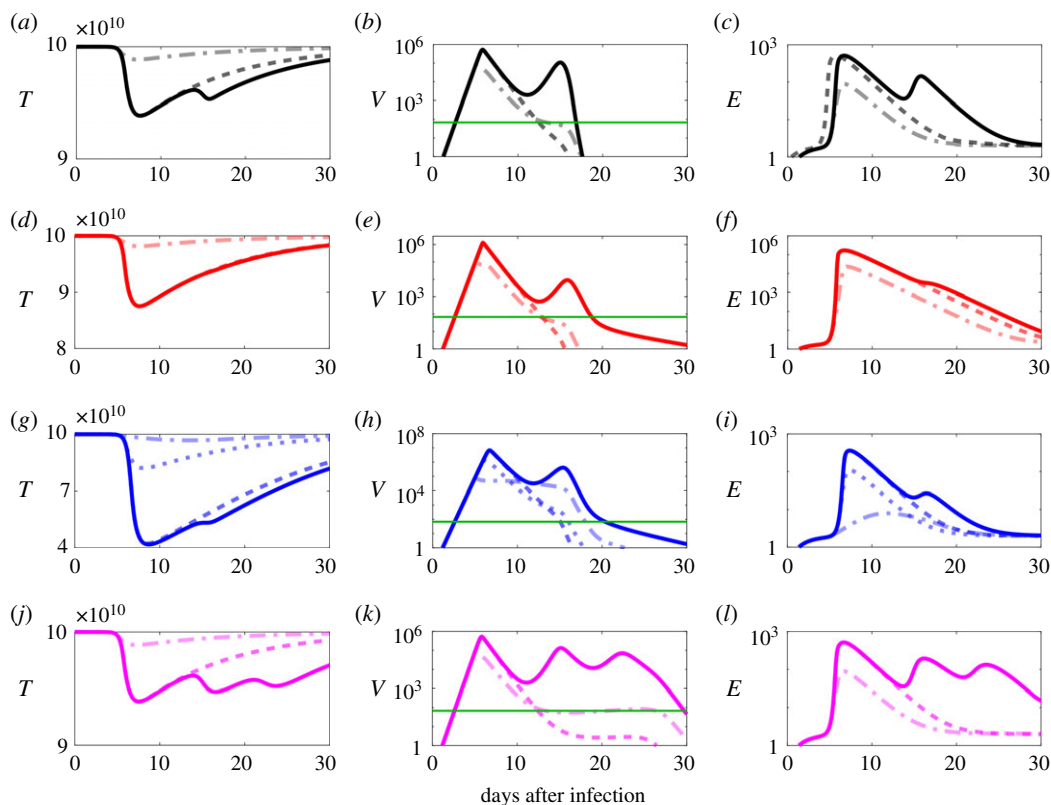
Figure 3. Antiviral treatment prevents the second viral peak and an earlier antiviral treatment start is more effective. Solid lines indicate progression of the infection in the absence of treatment as a control. Dashed, dotted and dash-dotted curves show the result of starting treatment at 7, 6 and 5 days post infection (dpi), respectively. Parameters are the median values of table 1 (black curves (a–c)). Red curves (d–f) correspond to the scenario of low removal rate of infected cells by effector cells ($\mu = 3.5 \times 10^{-4}$). Blue curves (g–i) illustrate the scenario of a low proliferation rate of effector cells ($\alpha = 5.4 \times 10^{-10}$), and magenta curves (j–l) of a low antibody proliferation rate ($r_A = 1$). The green line (horizontal line in (b), (e), (h) and (k)) indicates the viral detection limit. Note that for black, red and magenta the 6 dpi scenarios have similar curves to 7 dpi, so only 5 dpi and 7 dpi are visible in the plot.

clearance, we first generate a generic progression profile based on the data from all 12 patients, and then vary parameters pertinent to different aspects of the immune response in isolation in order to probe their impact on disease progression.

The median values from our parameter fitting were used to generate a generic progression profile from the 12 patient data as a control (black curves in figure 3a–c and electronic supplementary material, figure S5). This control curve reveals a characteristic two-peak behaviour for viral load (figure 3b), with antibodies passing the detection limit ($0.1\,\mathrm{ng\,ml}^{-1} = 4 \times 10^{8}$ molecules ml^{-1} [42]) after 14 days post infection (electronic supplementary material, figure S5d).

The cell-mediated immune response is captured in the equations by two factors: μ, the removal rate of infected cells by effector cells (T cells); and α, the proliferation rate of the effector cells. As λ_E/d_E is the basal level of effector cells, it is assumed to be constant for each patient [37]. Thus, α and μ are parameters that are probably varying in different patients. In particular, they would be expected to be lower in immunocompromised patients than for a patient with a healthy immune system [37,39,43,44]. Figure 3d (red curve; see also electronic supplementary material, figure S5) demonstrates that although reduction in the value of μ can increase the damage to healthy cells (T) slightly, this effect is much stronger when reducing α (figure 3g, blue curves). Even though decreasing either of these parameters causes a slower decline in viral load after the second peak (figure 3e,h), a smaller value of α in addition increases the maximum of both peaks. Figure 3j,k,l (magenta curves in electronic supplementary material, figure S5) model the case where just the humoral immune response is weakened, i.e. where the proliferation rate of antibodies r_A is reduced [42]. In this case, viral load shows three peaks, and the damage to healthy cells recovers only slowly. This demonstrates that each component of the immune response plays a different, and crucial role in the recovery process. In particular, in immunocompromised or elderly individuals who have a weakened immune response,

this could lead to significant tissue damage, with infections lasting much longer than for non-immunocompromised patients.

2.5. The impact of different therapeutic strategies on viral dynamics in patients with different types of immune response

In order to study the effects of antiviral therapy in the context of our intercellular model, we multiply the viral production rate p by $(1 - \epsilon)$, where $0 \leq \epsilon \leq 1$ is the drug efficacy [39,43,45,46]. As our intracellular model (figure 1c,d) suggests that starting treatment in the *latent period* is most effective, and would effectively block the production of virions, we set $\gamma = 0$ at the onset of treatment. This means that infected cells in the latent phase (L) do not transition to phase I, and begin shedding virions at a reduced rate (following a time lag τ) compared with cells that were already in phase I at the onset of treatment. However, as our numerical results show that the delayed model (electronic supplementary material, figure S6) has the same behaviour as the model without a time delay, i.e. $\tau = 0$, (figure 3), we set $\tau = 0$. Thus, we have the following equations for the numbers of infected cells and free virions:

$$\frac{dL}{dt} = \beta TV - \delta L - \gamma(1 - \theta(t - t_R))L - \mu LE,$$

$$\frac{dI}{dt} = \gamma(1 - \theta(t - t_R))L - \delta I - \mu IE, \tag{2.2}$$

$$\frac{dV}{dt} = p(1 - \epsilon)\theta(t - t_R)L + p(1 - \eta\theta(t - t_R))I - cV - kAV,$$

where $\theta(.)$ is the Heaviside function ($\theta(t) = 1$ for $t \geq 0$, and $\theta(t) = 0$ for $t < 0$), and t_R is the time when the antiviral treatment (remdesivir) is introduced. Cells in phase L produce virions at the reduced rate of $p(1 - \epsilon)$. Our intracellular model (figure 1c,d) suggests that starting therapy during the *latent period* can reduce the level of virions released by approximately 99% on average. We thus assume $\epsilon = 0.99$ for the efficacy of remdesivir in cells in phase L. This is a good approximation, as all values of ϵ calculated from figure 1c are above 98%, regardless of treatment start time. Cells that were already in the productively infectious phase (I) at the time of treatment start are assumed to produce virions at rate $p(1 - \eta)$, where $\eta \leq \epsilon$ is the efficacy of remdesivir in these cells. Figure 1c indicates that starting therapy during the productively infectious period can reduce the level of released virions by approximately 90% on average. Therefore, we set $\eta = 0.9$. We note that these values of ϵ and η are consistent with values used in previous models [6,7,21].

Figure 3a–c illustrates the impact of treatment on viral clearance in a patient who would most likely recover without treatment, as the parameters have been chosen as the median values of the 12 patients who have recovered from COVID-19 without treatment (table 1). In this generic scenario, a treatment start 7 days post infection (dpi), which is approximately the time of the first peak in viral load, prevents the second peak from occurring (black dashed lines in figure 3). An earlier treatment start at 6 dpi also leads to the same result. However, starting treatment even earlier at 5 dpi (black dash-dot lines in figure 3) also reduces the damage to healthy cells. Even though free virus declines slower in this case, the area under the viral load curve (AUC), an infection-related quantity commonly used to help the assessment of a treatment against acute viral diseases [47], is much smaller. In respiratory infections, even after viral clearance the immune response can cause respiratory and systemic symptoms in some incidences [47,48]. A treatment start at 5 dpi results in a reduction in the peak of immune response cells, suggesting that early treatment perhaps could mitigate against this.

In figure 3, solid red (figure 3d–f), blue (figure 3g–i) and magenta (figure 3j–l) curves indicate cases where different aspects of the immune response are weakened in isolation. In particular, the solid red (figure 3d–f) curves illustrate the case of a reduction in the removal rate of infected cells by effector cells μ by 99% with respect to the generic case ($\mu = 3.5 \times 10^{-4}$), the solid blue (figure 3g–i) curves that of a 92% reduced proliferation rate of effector cells α ($\alpha = 5.4 \times 10^{-10}$), and the solid magenta (figure 3j–l) curves correspond to a low antibody proliferation rate ($r_A = 1$ instead of 1.98). As in the generic case above, figure 3d–l indicate that in each case starting treatment 5 dpi reduces tissue damage, viral peak height and AUC significantly (electronic supplementary material, table S2), compared with treatment starts at 6 or 7 dpi, again emphasizing the importance of an early treatment start. However, early treatment increases the duration of infection compared with a later therapy start (figure 3h). This suggests that viral load could persist for a longer time in such patients, who may still be infectious.

Our intercellular model also enables the modelling of drugs that operate at the level of the immune response, rather than virus production in the intracellular milieu. As an example of a therapy option of this type, we study the impact of CP therapy on viral dynamics [5]. For this, we add a new variable to our model $(\tilde{A})$, which captures the antibodies that are administered as treatment. We assume that these antibodies remove virions at rate kf, where $0 \leq f \leq 1$, implying that they are at most as efficient as the antibodies that are being developed by the body over the course of the infection. The equations for the number of virions and antibodies thus have the form

$$\frac{\mathrm{d}V}{\mathrm{d}t} = pI - cV - kAV - \theta(t - t_{\mathrm{CP}})kf\tilde{A}V,$$

$$\frac{\mathrm{d}\tilde{A}}{\mathrm{d}t} = \theta(t - t_{\mathrm{CP}})(-kf\tilde{A}V - d_A\tilde{A}),$$

(2.3)

where $\tilde{A}(t) = 0$ for $t < t_{\mathrm{CP}}$ and $\tilde{A}(t_{\mathrm{CP}}) = \tilde{A}_m$, with $\tilde{A}_m$ representing the number of antibodies per ml that are administered as treatment. t_{CP} denotes the time at with the treatment is started, and $\theta(.)$ is the Heaviside function.

Our model enables the impact of CP therapy on viral dynamics to be studied for different treatment starts and doses, thus addressing the bottle-neck pointed out in the recent literature of finding the optimal dose and start for CP treatment [5]. Using again median values from table 1 to generate a generic patient profile as a control, and using three immunocompromised cases that are presented in figure 3 (red, blue and magenta curves, representing cases with reduced values for the immune response parameters μ, α and r_A, respectively) we studied the impact of CP therapy. Electronic supplementary material, figure S7 shows the minimum level of therapeutic antibodies $\tilde{A}_m$ that is needed to reduce the AUC by 25% and 50% as a function of the start of treatment (in dpi) and the factor f by which therapeutic antibodies are less efficient than those produced by the host during the infection. It indicates that the level of $\tilde{A}_m$ that is needed for an effective reduction in the AUC is at most around 3×10^{11} molecules ml^{-1}. This is in good agreement with clinical data, reporting a 200 ml dose of CP and $A_m = 4 \times 10^{12}$ molecules ml^{-1} (see Methods) [5,42,49]. Indeed, this implies that each dose would contain about 8×10^{14} molecules, resulting in $\tilde{A}_m = 2.6 \times 10^{11}$ molecules ml^{-1} on the basis of an average level of 3 l blood in the body [50]. Hence, a reduction of the AUC by 50% is achievable. Electronic supplementary material, figure S7 also shows that AUC reduction is comparable in the range $0.7 \leq f \leq 0.9$, therefore, we use the average value of this range ($f = 0.8$) in our calculations. Our conclusions are robust for efficiencies greater than or equal to 0.15, while for values of f below 0.15 the outcomes vary for different immunocompromised cases. Using these parameters, we present a comparative analysis between antiviral and CP therapy and explore their synergistic potential.

Figure 4 shows that similar to the case of antiviral therapy in figure 3, an early treatment start is more effective in the reduction of tissue damage and the level of AUC compared with a later therapy start (cf. electronic supplementary material, figure S8 for the equivalent of figure 3 for CP therapy; cf. electronic supplementary material, table S3 for AUC values). While figure 3 reveals scenarios in which an antiviral therapy does not mitigate against tissue damage (such as a later treatment start at 6 or 7 dpi), figure 4 shows that using CP therapy can reduce tissue damage even for those delayed treatment starts. Interestingly, figure 4 shows that starting CP therapy early can increase the duration of infection more than for antiviral therapy, implying that for an early treatment start using remdesivir is more effective. By contrast, for later treatment starts CP therapy reduces the viral load faster and decreases tissue damage compared with remdesivir therapy. Our model also enables us to probe the synergies of these treatments options. Figure 4c,f,i and l indicate that for an early treatment, combination therapy mitigates against a longer duration of the infection (cf. electronic supplementary material, table S4 for AUC values). However, for later treatment starts any synergistic effects are minimal and combination therapy has the same outcome as CP therapy in isolation. Thus, unless infection is detected early, e.g. though an efficient track and trace system, treatment would probably start at a time when CP therapy in isolation would be as effective as combination therapy.

Figure 5 indicates the impact of starting treatments after the onset of symptoms, i.e. the day on which symptoms were first reported by the 12 patients in the study [3] used for model fitting. Both treatments reduced the duration of the infection significantly (in 67% of the patients), enabling a faster recovery, or otherwise have no significant impact on the duration of the infection. However, in some cases in which the peak in viral load and the AUC are significantly reduced (electronic supplementary material, table S5), the treatments have not decreased the duration of infection. This figure also shows that there are cases for which the duration of infection is not reduced by one treatment, but would be reduced by
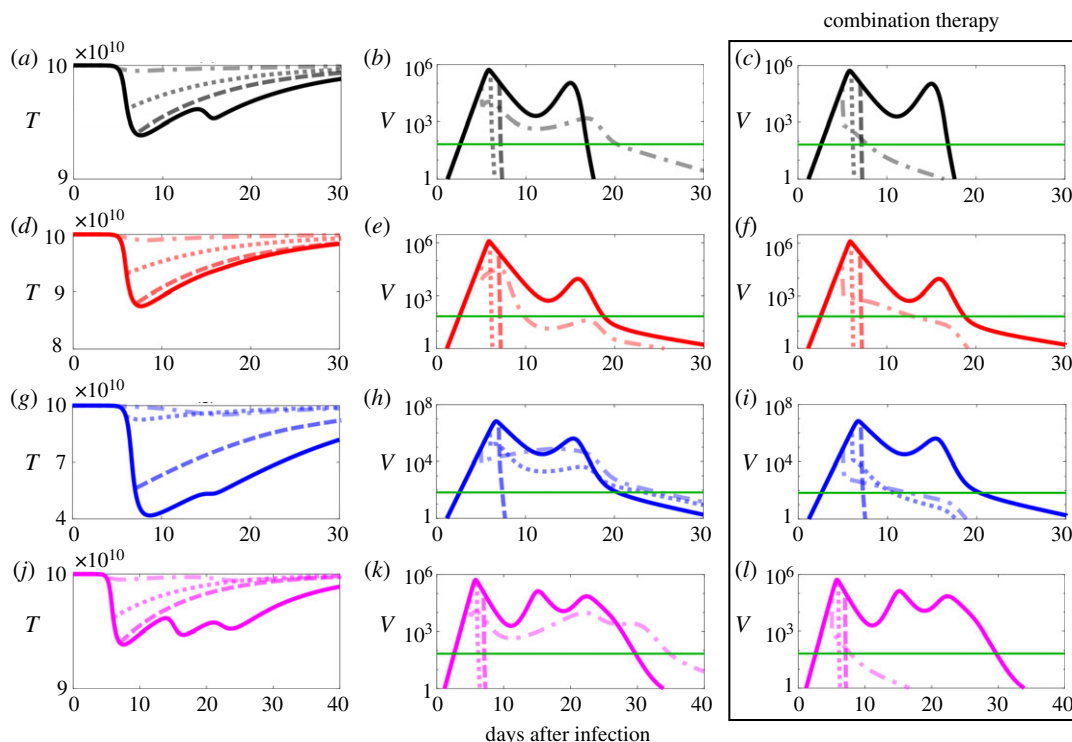
Figure 4. An early CP therapy increases the duration of infection more compared with an early antiviral therapy. Solid lines indicate progression of the infection in the absence of treatment as a control. Dashed, dotted and dash-dotted curves show the result of starting treatment at 7, 6 and 5 dpi, respectively. Parameters are the median values of table 1 (black curves $(a$–$c)$). Red curves $(d$–$f)$ correspond to the scenario of low removal rate of infected cells by effector cells $(\mu = 3.5 \times 10^{-4})$. Blue curves $(g$–$i)$ illustrate the scenario of a low proliferation rate of effector cells $(\alpha = 5.4 \times 10^{-10})$, and magenta curves $(j$–$l)$ of a low antibody proliferation rate $(r_A = 1)$. The green line (horizontal line in (b), (c) (e), (f), (h), (i), (k) and (l)) indicates the viral detection limit. First and second columns indicate the impact of CP therapy in isolation, while third column shows the impact of antiviral and CP therapy in combination.

combination therapy of both treatments. In the other cases, these treatment options have more or less similar effects, although CP therapy performs slightly better, and in these cases there is not a notable synergistic effect.

3. Discussion

The severe consequences of the COVID-19 pandemic demand a concerted interdisciplinary effort to identify novel antiviral solutions. Vaccination options against SARS-CoV-2 are actively pursued and a number of treatments are now in use in the clinics, but there are still many open questions regarding when and how best to administer these treatments, either in isolation or in combination. Whilst modelling of disease transmission has already played a key role in informing policy makers [51], models of within-host dynamics have not yet had a prominent role in combating the disease. There is a precedence of intracellular modelling for other viral diseases, such as hepatitis C virus [2]. However, such models cannot be readily transferred to coronaviral infection, as viral life cycles are very different. Here we introduce a within-host model of a SARS-CoV-2 infection that contains sufficient details specific to coronaviruses to enable antiviral strategies against SARS-CoV-2 to be compared and to analyse their synergies. We demonstrate this via a comparative analysis of an antiviral treatment (remdesivir) and CP therapy, which apart from steriod treatment are the most prominent forms of therapy currently used against COVID-19 infections. In particular, we compare disease progression for different treatment starts and dosages, and thus provide new insights into these therapeutic options.

Our analysis highlights, as expected and previously observed [6,7], that an early treatment start before the first peak in viral load can reduce both tissue damage and the peak viral load, especially when using a combination of both therapies. However, those models do not capture the impact of early treatment on the duration of the infection. Surprisingly, our model suggests that early treatment by either form of therapy alone can actually increase the duration of infection compared with a later
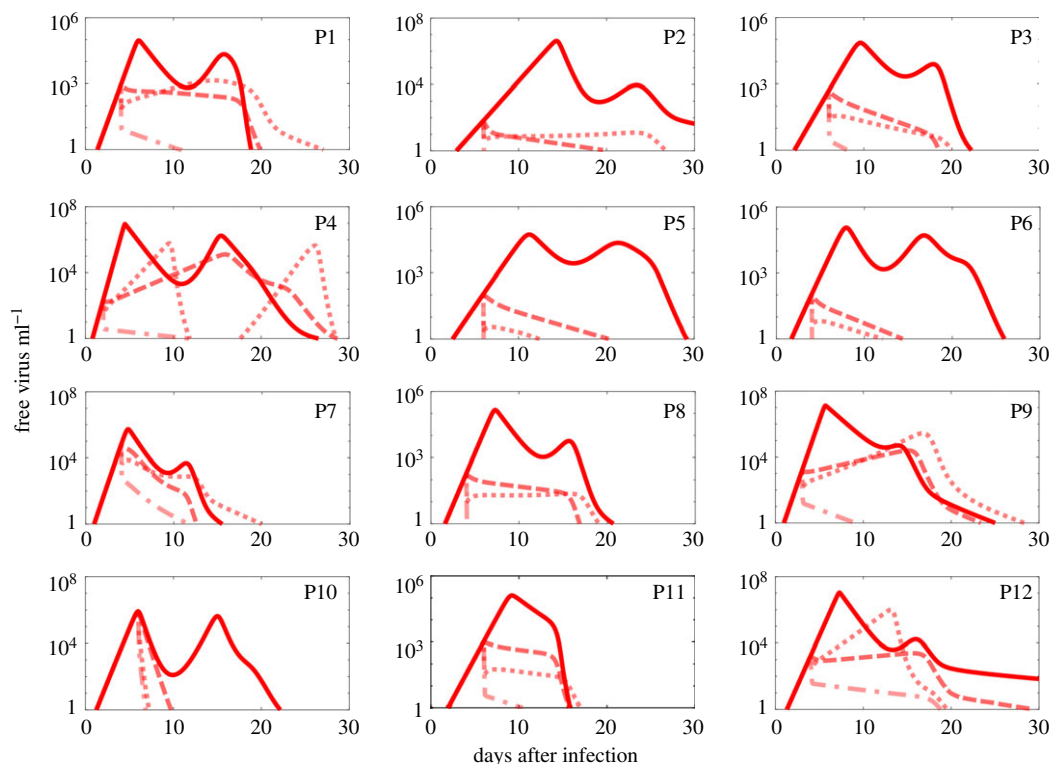
Figure 5. Starting treatment after the onset of symptoms reduces the peak in viral load and leads to faster viral clearance. Solid lines indicate the best fit to patient data. Dashed and dotted curves indicate the result of starting antiviral and CP therapy after the onset of symptoms, respectively, while dash-dotted curves indicate a combination therapy start after the onset of symptoms.

therapy start, probably because suppressing virus production results in a reduced immune response. This implies that even though early treatment accelerates the recovery process and reduces the peak in viral load, the infection may persist for a longer time than for later treatment starts, meaning that these patients may possibly still be infectious.

Our model has provided insights into disease progression for different doses and treatment starts for the CP therapy [5]. In particular, it enabled us to address a question recently raised in the literature as to the impact of dose and time of treatment on disease progression under CP treatment [5]. Our model also enabled us to perform a comparison between the antiviral treatment and CP therapy, and explore their potential synergistic effects. The model reveals that early into the infection an antiviral treatment using remdesivir could be more effective than CP therapy, and a combination therapy can significantly reduce the duration of infection. However, for later treatment starts, CP therapy appears to be more beneficial than antiviral therapy, and there are no longer any significant synergistic effects that would warrant combination therapy. These insights from our within-host model suggest that the time course of infection should be considered when deciding on an appropriate therapeutic response to a COVID-19 infection.

4. Methods

4.1. Intracellular modelling of SARS-CoV-2 infection

The first step in the viral lifecycle is the production of two polyproteins (pp1a and pp1ab) using the host cell ribosomes. The kinetics of ribosomes *in vivo* are studied using insights from a detailed stochastic model [52]. For synthesis of the polyproteins pp1a and pp1ab, host ribosomes (denoted by R in electronic supplementary material, figure S1b) reversibly bind to (+)RNA with binding/unbinding rates r_{on} and r_{off}

$$(+)\text{RNA} + \text{R} \underset{r_{off}}{\overset{r_{on}}{\rightleftharpoons}} \text{R} : (+)\text{RNA}.$$
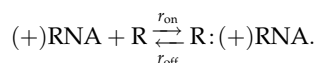
We model the kinetic steps involved in ribosome initiation and transition to the elongation state (Ri_{1a}: (+)RNA) that occur subsequent to ribosomal binding to the (+)RNA to produce pp1a as a single kinetic step with rate r_{in}.

$$R: (+)RNA \xrightarrow{r_{in}} Ri_{1a}: (+)RNA.$$
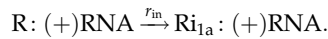
The ribosome then translates the pp1a gene (ORF1a) at rate t_{1a}. After translation of the pp1a gene, the ribosome can either frameshift −1 nt to the ORF1b reading frame, translating the polyprotein pp1ab, or terminate, releasing the polyprotein pp1a [18]. We model the −1 ribosomal frameshift as a reaction with rate $q \times t_f$ and the termination at ORF1a as a reaction with rate $(1-q)t_f$. If the ribosome successfully frameshifts, it completes translation of the ORF1b reading frame with rate t_{1b}, terminates, and releases the polyprotein pp1ab
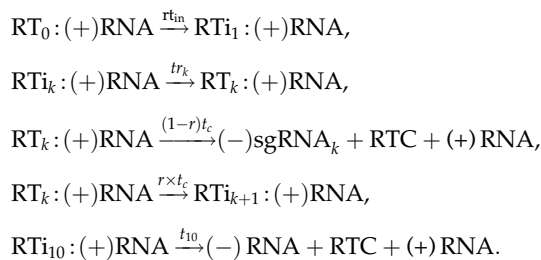
$$Ri_{1a}: (+)RNA \xrightarrow{t_{1a}} R_{1a}: (+)RNA,$$

$$R_{1a}: (+)RNA \xrightarrow{(1-q)t_f} pp1a + R + (+)RNA,$$

$$R_{1a}: (+)RNA \xrightarrow{q \times t_f} Ri_{1b}: (+)RNA,$$

$$Ri_{1b}: (+)RNA \xrightarrow{t_{1b}} pp1ab + R + (+)RNA.$$
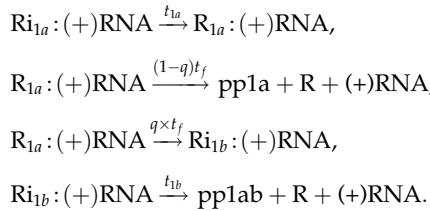
The polyproteins pp1a and pp1ab form RTC at rate f_{rt}

$$pp1a + pp1ab \xrightarrow{f_{rt}} RTC.$$

The transcription of gRNA which leads to the formation of −gRNA and nine −sgRNAs is modelled as illustrated in the electronic supplementary material, figure S2. RTC (denoted by RTC in the electronic supplementary material, figure S2) binds to the genome with binding/unbinding rates rt_{on} and rt_{off}
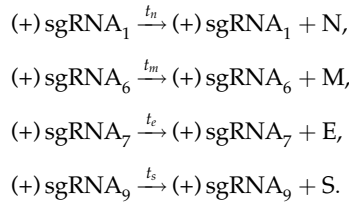
$$(+)RNA + RTC \underset{rt_{off}}{\overset{rt_{on}}{\rightleftharpoons}} RT_0: (+)RNA.$$
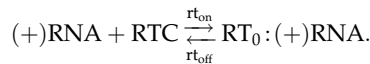
The full-length genome contains functional transcription-regulating sequence (TRS) motifs which are found at the 3′ end of the leader (leader TRS) and in front of each of the nine ORFs (electronic supplementary material, figure S1a) [20]. During transcription of the full-length minus strand by the RTC, the process can terminate at one of these TRS motifs, resulting in one of the nine negative sgRNA being produced. In our model, when an RTC encounters TRS motif number k, it will continue the elongation of the negative strand with rate $r \times t_c$, and terminate with rate $(1 - r)t_c$, resulting in the production of $(-)sgRNA_k$

$$RT_0: (+)RNA \xrightarrow{rt_{in}} RTi_1: (+)RNA,$$

$$RTi_k: (+)RNA \xrightarrow{tr_k} RT_k: (+)RNA,$$

$$RT_k: (+)RNA \xrightarrow{(1-r)t_c} (-)sgRNA_k + RTC + (+)RNA,$$

$$RT_k: (+)RNA \xrightarrow{r \times t_c} RTi_{k+1}: (+)RNA,$$

$$RTi_{10}: (+)RNA \xrightarrow{t_{10}} (-)RNA + RTC + (+)RNA.$$

Here, tr_k is the rate of RTC transcription between the TRS at site $k-1$ and site k (electronic supplementary material, figure S2) and each $(-)sgRNA_k$ for $k = 1, 2, \ldots, 9$, corresponds to sgRNAs for N, 8, 7b, 7a, 6, M, E, 3a, S $(-)$sgRNAs, respectively, whereas the $k = 10$ state with transcription rate t_{10} denotes the rate to transcribe the remaining length of 22 kb of RNA upstream of the structural genes. This last step is responsible for the creation of full-length $(-)$RNA. Then $(-)$sgRNAs and $(-)$RNA serve as templates for $(+)$sgRNAs and viral genome synthesis, respectively. The negative RNAs bind to RTC and produce positive RNAs (electronic supplementary material, equation S1).

$(+)sgRNA_1$, $(+)sgRNA_6$, $(+)sgRNA_7$ and $(+)sgRNA_9$ encode structural proteins N, M, E and S, respectively, which are involved in the formation of new virions [21]. We assume that free ribosomes

are at an equilibrium level, where +sgRNAs are saturated with available ribosomes and produce protein at constant rates t_n, t_m etc.
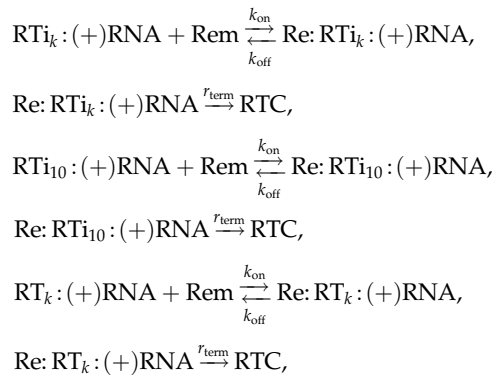
$$(+)\,sgRNA_1 \xrightarrow{t_n} (+)\,sgRNA_1 + N,$$

$$(+)\,sgRNA_6 \xrightarrow{t_m} (+)\,sgRNA_6 + M,$$

$$(+)\,sgRNA_7 \xrightarrow{t_e} (+)\,sgRNA_7 + E,$$

$$(+)\,sgRNA_9 \xrightarrow{t_s} (+)\,sgRNA_9 + S.$$

The budding of a virion is modelled as a single reaction with budding rate k_{bud} as follows [2,16]:

$$(+)\,RNA + 300S + 2000M + 1000N + 100E \xrightarrow{k_{bud}} virion.$$
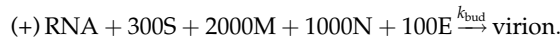
4.2. Modelling of antiviral strategy

Remdesivir acts as a nucleoside analogue that mimics the adenosine structure [32]. During the replication process, RTC may insert remdesivir molecules rather than adenine, which caps the strand and stops the replication process at rate r_{term} [25]. In order to model the impact of this drug, we assume that complexes with RTC in our model can bind (and subsequently unbind from) remdesivir molecules (Rem). Thus, the reactions have the following form:

$$RTi_k : (+)RNA + Rem \underset{k_{off}}{\overset{k_{on}}{\rightleftarrows}} Re : RTi_k : (+)RNA,$$

$$Re : RTi_k : (+)RNA \xrightarrow{r_{term}} RTC,$$

$$RTi_{10} : (+)RNA + Rem \underset{k_{off}}{\overset{k_{on}}{\rightleftarrows}} Re : RTi_{10} : (+)RNA,$$

$$Re : RTi_{10} : (+)RNA \xrightarrow{r_{term}} RTC,$$

$$RT_k : (+)RNA + Rem \underset{k_{off}}{\overset{k_{on}}{\rightleftarrows}} Re : RT_k : (+)RNA,$$

$$Re : RT_k : (+)RNA \xrightarrow{r_{term}} RTC,$$

where $k = 1, 2, \ldots, 9$.

4.3. Patient data

Our patient data comprise the first 18 confirmed patients who reported COVID-19 infection in Singapore [3]. Nasopharyngeal swabs were collected for up to 30 days since onset of symptoms. Five patients received lopinavir–ritonavir treatment, and in one patient viral load was detectable only twice, and these six patients were therefore excluded from the analysis. The viral loads were reported in cycle threshold (Ct) values, which is inversely proportional to the logarithm of the viral RNA copy number ($\log(V) = -0.3231Ct + 14.11$) [35]. We converted Ct values to viral copies per millilitre. In model fitting, viral load values under the detection threshold were set at the detection limit (Ct = 38).

4.4. Intercellular model parameter estimation

COVID-19 is a respiratory illness, so we assume that modelling insights from influenza models are applicable. In influenza, at approximately 5–7 dpi mitoses are detected at the basal cell layer, and regeneration of the epithelium begins. Complete resolution of the epithelial takes up to one month [36]. We therefore assume that the maximum proliferation rate for uninfected cells is small, and that $r_T = 0.1\,d^{-1}$. The number of host cells that express ACE-2 and transmembrane serine protease (TMPRSS) is approximately equal to 10^{11} ($T_m = 10^{11}$) [16], and we use $T(0) = T_m$. As SARS-CoV-2 is a novel infection, we assume that $E(0) = 0$ and that the basal level of effector cells is low ($\lambda_E = 1$ and $d_E = 0.5\,d^{-1}$) [53]. However, considering a higher basal level does not change model outcomes regarding the viral dynamics, as α and μ, the proliferation rates of effector cells and removal rate of

infected cells by effector cells, are estimated using viral load data fitting. Note that increasing λ and decreasing μ simultaneously does result in the same viral dynamics, although it will change the value of the peak in effector cells. Since data are only available regarding viral load, we decided to fix the basal level of effector cells before finding other parameters [42,53]. Initially, there is no specific antibody, therefore $A(0) = 0$ and $d_A = 0.033\,\text{d}^{-1}$ [42]. We use 1 µg ml^{-1} immunoglobulin G (IgG) positive control as a strong positive standard [49]. Thus, we assume $A_m = 1\,\mu\text{g ml}^{-1} = 4 \times 10^{12}$ molecules ml^{-1}. Although we are setting the individual's antibody carrying capacity to a fixed value [42], we also checked that variation of the parameter does not impact the qualitative results and therefore all conclusions remain valid. d_A is measured for HBV infection, but it has been shown that $r_A A(1 - A/A_m) - d_A A$ is equivalent to a logistic growth of antibodies with growth rate $\rho_A = r_A - d_A$ [42]. Since we are fitting r_A, fixing d_A does not have a significant impact on the model. The same argument is valid for d_E, and as we are assuming a fixed basal level (λ_E/d_E), changing d_E would not have a significant effect on our results.

The patient data used is only available from the time after onset of symptoms, and the initial viral load at the start of the infection is not recorded. We therefore estimate the value $V(0)$ assuming the infection is transmitted via droplets. The average number of expelled droplets during talking is assumed to be 1000 [54,55]. It has also been reported that more than 50% of droplets have a size range between 50 and 75 µm [55]. Thus, the average volume in expelled droplets during talking is equal to 1.1×10^{-4} ml. The median level of viral load on the day of symptom onset in patients in this study is estimated as 5×10^3 virion ml^{-1} [56]. We assume that infected individuals infect others before the onset of symptoms, and we therefore assume an average level of 10^3 virion ml^{-1} are available for transmission. Thus, assuming $V(0) = 0.1$ virion ml^{-1} appears to be a reasonable choice [6]. This value is also comparable to those used in modelling of influenza [57].

Since structural identifiability is a necessary condition for model fitting, we used the method by Castro & de Boer [58] to show that our model (2.1) is structurally identifiable (see electronic supplementary material, section S3 for more detail). We estimate the remaining parameters and the *incubation period* (the time between the beginning of the infection and the onset of symptoms) by fitting V from the model (2.1) to patient data individually in Matlab using the method in Ciupe *et al.* [42] which uses the minimum search function for data fitting. Although we fitted patient data individually, which is suboptimal compared to population fitting using mixed effects, the outcomes of the model were in agreement with clinically measured values, such as the incubation period and the onset of appearance of antibodies in the body. The resulting parameter values are presented in table 1. Decreasing/increasing of $V(0)$ ($V(0) = 0.01$ virion ml^{-1} or $V(0) = 1$ virion ml^{-1}) does not change the estimated values of parameters significantly and only changes the estimated *incubation period* by ±1 day. Additionally, we used residual bootstrapping to provide 95% confidence intervals (CIs) for the parameter estimates following [37] (electronic supplementary material, table S2). For each set of patient data $\{V_1, V_2, \ldots, V_n\}$, we calculated the normalised residuals $\epsilon_i = V_i/\overline{V}_i, i = 1, 2, \ldots, n$, where $\{\overline{V}_1, \overline{V}_2, \ldots, \overline{V}_n\}$ denotes the viral load values predicted by the model. We then created the set $\{V_1^*, V_2^*, \ldots, V_n^*\}$ where $V_i^* = \overline{V}_i \times \epsilon_j$ for ϵ_j randomly chosen to be any of the normalised residuals or 1, the latter to include the option that the data remains unchanged. We created 50 samples and fitted each individually to the data. We then calculated the 95% CI for each given parameter across the 50 parameter sets (electronic supplementary material, table S2). We generated 500 simulations based on randomly chosen parameters from the 50 parameter sets, and then used these curves to calculate the 95% CI for each patient (see red shaded areas in electronic supplementary material, figure S4). As the 95% CIs have negligible width compared with the widths of the curves, given the logarithmic scale, we also added the mean plus/minus standard deviation as shaded green areas in order to reflect the noise in the data, especially for P4 and P6. We note that the predicted two-peak behaviour is consistent with observations in Wölfel *et al.* [59], and indeed is expected in any model that includes the adaptive immune response [60].

References

1. Lai CC, Shih TP, Ko WC, Tang HJ, Hsueh PR. 2020 Severe acute respiratory syndrome coronavirus 2 (SARS-CoV-2) and coronavirus disease-2019 (COVID-19): the epidemic and the challenges. *Int. J. Antimicrob. Agents* **55**, 105924. (doi:10.1016/j.ijantimicag.2020.105924)

2. Aunins TR, Marsh KA, Subramanya G, Uprichard SL, Perelson AS, Chatterjee A. 2018 Intracellular hepatitis C virus modeling predicts infection dynamics and viral protein mechanisms. *J. Virol.* **92**, e02098–17. (doi:10.1128/JVI.02098-17)

3. Young BE *et al.* 2020 Epidemiologic features and clinical course of patients infected with SARS-CoV-2 in Singapore. *JAMA* **323**, 1488–1494. (doi:10.1001/jama.2020.3204)

4. Beigel JH *et al.* 2020 Remdesivir for the treatment of Covid-19—preliminary report. *N. Engl. J. Med.* **383**, 1813–1826. (doi:10.1056/NEJMoa2007764)

5. Duan K *et al.* 2020 Effectiveness of convalescent plasma therapy in severe COVID-19 patients. *Proc. Natl Acad. Sci. USA* **117**, 9490–9496. (doi:10.1073/pnas.2004168117)

6. Gonçalves A *et al.* 2020 Timing of antiviral treatment initiation is critical to reduce SARS-CoV-2 viral load. *CPT Pharmacometrics Syst. Pharmacol.* **9**, 509–514. (doi:10.1002/psp4.12543)

7. Iwanami S *et al.* 2020 Detection of significant antiviral drug effects on COVID-19 with reasonable sample sizes in randomized controlled trials: a modeling study. *PLoS Med.* **18**, e1003660. (doi:10.1371/journal.pmed.1003660)

8. Nowak M, May RM. 2000 *Virus dynamics*. Oxford, UK: Oxford University Press.

9. Andrew SM, Baker CT, Bocharov GA. 2007 Rival approaches to mathematical modelling in immunology. *J. Comput. Appl. Math.* **205**, 669–686. (doi:10.1016/j.cam.2006.03.053)

10. Joyner MJ *et al.* 2020 Early safety indicators of COVID-19 convalescent plasma in 5000 patients. *J. Clin. Invest.* **130**, 4791–4797. (doi:10.1172/JCI140200)

11. Joyner MJ *et al.* 2020 Safety update: COVID-19 convalescent plasma in 20 000 hospitalized patients. *Mayo Clin. Proc.* **95**, 1888–1897. (doi:10.1016/j.mayocp.2020.06.028)

12. Ahn JY *et al.* 2020 Use of convalescent plasma therapy in two COVID-19 patients with acute respiratory distress syndrome in Korea. *J. Korean Med. Sci.* **35**, e149. (doi:10.3346/jkms.2020.35.e149)

13. Ye M, Fu D, Ren Y, Wang F, Wang D, Zhang F, Xia X, Lv T. 2020 Treatment with convalescent plasma for COVID-19 patients in Wuhan, China. *J. Med. Virol.* **92**, 1890–1901. (doi:10.1002/jmv.25882)

14. Gharbharan A *et al.* 2021 Effects of potent neutralizing antibodies from convalescent plasma in patients hospitalized for severe SARS-CoV-2 infection. *Nat. Commun.* **12**, 3189. (doi:10.1038/s41467-021-23469-2)

15. Khulood D, Adil MS, Sultana R, Nimra. 2020 Convalescent plasma appears efficacious and safe in COVID-19. *Ther. Adv. Infect. Dis.* **7**, 2049936120957931. (doi:10.1177/2049936120957931)

16. Bar-On YM, Flamholz A, Phillips R, Milo R. 2020 SARS-CoV-2 (COVID-19) by the numbers. *Elife* **9**, e57309. (doi:10.7554/eLife.57309)

17. Fehr AR, Perlman S. 2015 Coronaviruses: an overview of their replication and pathogenesis. In *Coronaviruses* (eds HJ Maier, E Bickerton, P Britton), pp. 1–23. Berlin, Germany: Springer.

18. Nakagawa K, Lokugamage KG, Makino S. 2016 Viral and cellular mRNA translation in coronavirus-infected cells. *Adv. Virus Res.* **96**, 165–192. (doi:10.1016/bs.aivir.2016.08.001)

19. de Wit E, van Doremalen N, Falzarano D, Munster VJ. 2016 SARS and MERS: recent insights into emerging coronaviruses. *Nat. Rev. Microbiol.* **14**, 523. (doi:10.1038/nrmicro.2016.81)

20. Sawicki SG, Sawicki DL, Siddell SG. 2007 A contemporary view of coronavirus transcription. *J. Virol.* **81**, 20–29. (doi:10.1128/JVI.01358-06)

21. Kim D, Lee JY, Yang JS, Kim JW, Kim VN, Chang H. 2020 The architecture of SARS-CoV-2 transcriptome. *Cell* **181**, 914–921. (doi:10.1016/j.cell.2020.04.011)

22. Gillespie DT. 1977 Exact stochastic simulation of coupled chemical reactions. *J. Phys. Chem.* **81**, 2340–2361. (doi:10.1021/j100540a008)

23. Dimelow RJ, Wilkinson SJ. 2009 Control of translation initiation: a model-based analysis from limited experimental data. *J. R. Soc. Interface* **6**, 51–61. (doi:10.1098/rsif.2008.0221)

24. Te Velthuis AJW, Arnold JJ, Cameron CE, Snijder EJ. 2010 The RNA polymerase activity of SARS-coronavirus nsp12 is primer dependent. *Nucleic Acids Res.* **38**, 203–214. (doi:10.1093/nar/gkp904)

25. Zhang L, Zhou R. 2020 Structural basis of the potential binding mechanism of remdesivir to SARS-CoV-2 RNA-dependent RNA polymerase. *J. Phys. Chem. B* **124**, 6955–6962. (doi:10.1021/acs.jpcb.0c04198)

26. Gordon CJ, Tchesnokov EP, Feng JY, Porter DP, Götte M. 2020 The antiviral compound remdesivir potently inhibits RNA-dependent RNA polymerase from Middle East respiratory syndrome coronavirus. *J. Biol. Chem.* **295**, 4773–4779. (doi:10.1074/jbc.AC120.013056)

27. Baranov PV, Henderson CM, Anderson CB, Gesteland RF, Atkins JF, Howard MT. 2005 Programmed ribosomal frameshifting in decoding the SARS-CoV genome. *Virology* **332**, 498–510. (doi:10.1016/j.virol.2004.11.038)

28. Brierley I *et al.* 1987 An efficient ribosomal frame-shifting signal in the polymerase-encoding region of the coronavirus IBV. *EMBO J.* **6**, 3779–3785. (doi:10.1002/j.1460-2075.1987.tb02713.x)

29. Herald J, Siddell SG. 1993 An 'elaborated' pseudoknot is required for high frequency frameshifting during translation of HCV 229E polymerase mRNA. *Nucleic Acids Res.* **21**, 5838–5842. (doi:10.1093/nar/21.25.5838)

30. Plant EP, Dinman JD. 2006 Comparative study of the effects of heptameric slippery site composition on −1 frameshifting among different eukaryotic systems. *RNA* **12**, 666–673. (doi:10.1261/rna.2225206)

31. Irigoyen N, Firth AE, Jones JD, Chung BYW, Siddell SG, Brierley I. 2016 High-resolution analysis of coronavirus gene expression by RNA sequencing and ribosome profiling. *PLoS Pathog.* **12**, e1005473. (doi:10.1371/journal.ppat.1005473)

32. Warren TK *et al.* 2016 Therapeutic efficacy of the small molecule GS-5734 against Ebola virus in rhesus monkeys. *Nature* **531**, 381–385. (doi:10.1038/nature17180)

33. Agostini ML *et al.* 2018 Coronavirus susceptibility to the antiviral remdesivir (GS-5734) is mediated by the viral polymerase and the proofreading exoribonuclease. *mBio* **9**, e00221-18. (doi:10.1128/mBio.00221-18)

34. Fatehi F, Bingham RJ, Dykeman EC, Patel N, Stockley PG, Twarock R. 2020 An intracellular model of hepatitis B viral infection: an in silico platform for comparing therapeutic strategies. *Viruses* **13**, 11. (doi:10.3390/v13010011)

35. Zou L *et al.* 2020 SARS-CoV-2 viral load in upper respiratory specimens of infected patients. *N. Engl. J. Med.* **382**, 1177–1179. (doi:10.1056/NEJMc2001737)

36. Wright PF, Webster RG. 2001 Orthomyxoviruses. In *Fields virology*, 4th edn (eds BN Fields, DM Knipe), pp. 1533–1579. Philadelphia, PA: Lippincott Williams & Wilkins.

37. Ciupe SM, Ribeiro RM, Nelson PW, Dusheiko G, Perelson AS. 2007 The role of cells refractory to productive infection in acute hepatitis B viral dynamics. *Proc. Natl Acad. Sci. USA* **104**, 5050–5055. (doi:10.1073/pnas.0603626104)

38. Handel A, Longini Jr IM, Antia R. 2010 Towards a quantitative understanding of the within-host dynamics of influenza A infections. *J. R. Soc. Interface* **7**, 35–47. (doi:10.1098/rsif.2009.0067)

39. Fatehi Chenar F, Kyrychko YN, Blyuss KB. 2018 Mathematical model of immune response to hepatitis B. *J. Theor. Biol.* **447**, 98–110. (doi:10.1016/j.jtbi.2018.03.025)

40. Lauer SA *et al.* 2020 The incubation period of coronavirus disease 2019 (COVID-19) from publicly reported confirmed cases: estimation and application. *Ann. Intern. Med.* **172**, 577–582. (doi:10.7326/M20-0504)

41. Harcourt J *et al.* 2020 Severe acute respiratory syndrome coronavirus 2 from patient with coronavirus disease, United States. *Emerg. Infect. Dis.* **26**, 1266–1273. (doi:10.3201/eid2606.200516)

42. Ciupe SM, Ribeiro RM, Perelson AS. 2014 Antibody responses during hepatitis B viral infection. *PLoS Comput. Biol.* **10**, e1003730. (doi:10.1371/journal.pcbi.1003730)

43. Guedj J, Dahari H, Rong L, Sansone ND, Nettles RE, Cotler SJ, Layden TJ, Uprichard SL, Perelson AS. 2013 Modeling shows that the NS5A inhibitor daclatasvir has two modes of

action and yields a shorter estimate of the hepatitis C virus half-life. *Proc. Natl Acad. Sci. USA* **110**, 3991–3996. (doi:10.1073/pnas. 1203110110)

44. Conway JM, Perelson AS. 2015 Post-treatment control of HIV infection. *Proc. Natl Acad. Sci. USA* **112**, 5467–5472. (doi:10.1073/pnas. 1419162112)

45. Dahari H, Shudo E, Ribeiro RM, Perelson AS. 2009 Modeling complex decay profiles of hepatitis B virus during antiviral therapy. *Hepatology* **49**, 32–38. (doi:10.1002/hep.22586)

46. Kim HY, Kwon HD, Jang TS, Lim J, Lee HS. 2012 Mathematical modeling of triphasic viral dynamics in patients with HBeAg-positive chronic hepatitis B showing response to 24-week clevudine therapy. *PLoS ONE* **7**, e50377. (doi:10.1371/journal.pone.0050377)

47. Vegvari C *et al.* 2016 How can viral dynamics models inform endpoint measures in clinical trials of therapies for acute viral infections? *PLoS ONE* **11**, e0158237. (doi:10.1371/journal.pone. 0158237)

48. Ison MG *et al.* 2010 End points for testing influenza antiviral treatments for patients at high risk of severe and life-threatening disease. *J. Infect. Dis.* **201**, 1654–1662. (doi:10.1086/652498)

49. Sun B *et al.* 2020 Kinetics of SARS-CoV-2 specific IgM and IgG responses in COVID-19 patients. *Emerg. Microbes Infect.* **9**, 940–948. (doi:10.1080/22221751.2020.1762515)

50. Murray JM, Goyal A. 2015 In silico single cell dynamics of hepatitis B virus infection and clearance. *J. Theor. Biol.* **366**, 91–102. (doi:10. 1016/j.jtbi.2014.11.020)

51. Bertozzi AL, Franco E, Mohler G, Short MB, Sledge D. 2020 The challenges of modeling and forecasting the spread of COVID-19. *Proc. Natl Acad. Sci. USA* **117**, 16 732–16 738. (doi:10. 1073/pnas.2006520117)

52. Dykeman EC. 2020 A stochastic model for simulating ribosome kinetics *in vivo*. *PLoS Comput. Biol.* **16**, e1007618. (doi:10.1371/ journal.pcbi.1007618)

53. Ciupe SM, Ribeiro RM, Nelson PW, Perelson AS. 2007 Modeling the mechanisms of acute hepatitis B virus infection. *J. Theor. Biol.* **247**, 23–35. (doi:10.1016/j.jtbi.2007.02.017)

54. Loudon RG, Roberts RM. 1967 Droplet expulsion from the respiratory tract. *Am. Rev. Respir. Dis.* **95**, 435–442.

55. Xie X, Li Y, Sun H, Liu L. 2009 Exhaled droplets due to talking and coughing. *J. R. Soc. Interface* **6**, S703–S714. (doi:10.1098/rsif.2009.0388.focus)

56. Ejima K *et al.* 2020 Inferring timing of infection using within-host SARS-CoV-2 infection dyna (i) text mics model: are 'Imported Cases' truly imported? *medRxiv*. (doi:10.1101/2020.03.30. 20040519)

57. Pawelek KA, Huynh GT, Quinlivan M, Cullinane A, Rong L, Perelson AS. 2012 Modeling within-host dynamics of influenza virus infection including immune responses. *PLoS Comput. Biol.* **8**, e1002588. (doi:10.1371/journal.pcbi. 1002588)

58. Castro M, de Boer RJ. 2020 Testing structural identifiability by a simple scaling method. *PLoS Comput. Biol.* **16**, e1008248. (doi:10.1371/ journal.pcbi.1008248)

59. Wölfel R *et al.* 2020 Virological assessment of hospitalized patients with COVID-2019. *Nature* **581**, 465-469.

60. Perelson AS, Ke R. 2021 Mechanistic Modeling of SARS-CoV-2 and Other Infectious Diseases and the Effects of Therapeutics. *Clin. Pharmacol*.

61. Fatehi F, Bingham RJ, Dykeman EC, Stockley PG, Twarock R. 2021 COVID-19 patient data from a study in Singapore curated for input into an in silico infection model. Dryad Digital Repository. (https://doi.org/10.5061/dryad.sn02v6x38)